RESEARCH ARTICLE | MAY 12 2023

Shape-induced crystallization of binary DNA-functionalized nanocubes 🟦 Ⓕ ⊘

Yunhan Zhang ✉ ⓘD ; Giuliana Giunta ⓘD ; Haojun Liang ⓘD ; Marjolein Dijkstra ✉ ⓘD

Check for updates

View Online   Export Citation   CrossMark

The Journal of Chemical Physics

Special Topic: Algorithms and Software for Open Quantum System Dynamics

Submit Today

AIP Publishing

AIP Publishing

Shape-induced crystallization of binary DNA-functionalized nanocubes SCI F

View Online   Export Citation   CrossMark

Yunhan Zhang,[1,2,a)] iD Giuliana Giunta,[2,b)] iD Haojun Liang,[1] iD
and Marjolein Dijkstra[2,a)] iD

AFFILIATIONS

[1] Department of Polymer Science and Engineering, CAS Key Laboratory of Soft Matter Chemistry,
iChEM (Collaborative Innovation Center of Chemistry for Energy Materials), University of Science and Technology of China,
Hefei, Anhui 230026, People's Republic of China
[2] Soft Condensed Matter, Debye Institute for Nanomaterials Science, Utrecht University,
Princetonplein 5, 3584 CC Utrecht, The Netherlands

[a)]Author to whom correspondence should be addressed: zhangyh8@mail.ustc.edu.cn and m.dijkstra@uu.nl
[b)]Current address: BASF SE, Carl-Bosch-Strasse 38, 67056 Ludwigshafen am Rhein, Germany.

ABSTRACT

Leveraging the anisotropic shape of DNA-functionalized nanoparticles holds potential for shape-directed crystallization of a wide collection of superlattice structures. Using coarse-grained molecular dynamics simulations, we study the self-assembly of a binary mixture of cubic gold nanoparticles, which are functionalized by complementary DNA strands. We observe the spontaneous self-assembly of simple cubic (SC), plastic body-centered tetragonal (pBCT), and compositionally disordered plastic body-centered tetragonal (d-pBCT) phases due to hybridization of the DNA strands. We systematically investigate the effect of length, grafting density, as well as rigidity of the DNA strands on the self-assembly behavior of cubic nanoparticles. We measure the potential of mean force between DNA-functionalized nanocubes for varying rigidity of the DNA strands and DNA lengths. Using free-energy calculations, we find that longer and flexible DNA strands can lead to a phase transformation from SC to the pBCT phase due to a gain in entropy arising from the orientational degrees of freedom of the nanocubes in the pBCT phase. Our results may serve as a guide for self-assembly experiments on DNA-functionalized cubic nanoparticles.

Published under an exclusive license by AIP Publishing. https://doi.org/10.1063/5.0148139

I. INTRODUCTION

Inspired by nature, self-assembly has been widely used in nanotechnology to manufacture and design nanostructured materials.[1] In the past few decades, scientists have exploited the wide variety of available colloidal building blocks and have self-assembled them into a diversity of structural arrangements that can be used for advanced functional materials in fields as diverse as aviation and space,[2] solar hydrogen,[3] fuel cells,[4] biosensors,[5] power generation,[6] and medical materials.[7]

In recent years, we have seen two exciting developments that significantly increased the diversity of self-assembled colloidal structures. In the first approach, the shape of the colloidal particles is exploited to assemble a vast array of structures. Huge research efforts have been devoted on investigating the effect of particle shape on the entropy-driven self-assembly of hard particles[8–11] and on predicting

their densest structures.[12–14] These studies demonstrate that hard-particle systems can self-assemble into an astonishing diversity of structures, such as crystal and plastic crystal phases, liquid crystals, and even quasicrystals, depending on their precise particle shape and thermodynamic state point.

Another very promising self-assembly strategy dates back to the mid-1990s when single-stranded DNA oligonucleotides with a well-defined length and sequence were attached to individual nanoparticles, and the Watson–Crick base-pairing interactions of complementary DNA strands were exploited to program the interparticle interactions and self-assembly of nanoparticles.[15,16] These pioneering works represented the first well-characterized formation of spherical nucleic acid (SNA) conjugates. The functionalization of nanoparticles with DNA can be exploited to control and direct colloidal self-assembly,[15–19] and hence, the SNA conjugates are also referred to as "programmable atom-equivalents" (PAEs). Similar to

atoms, these PAEs are capable to assemble into a wide variety of well-ordered superlattices,[20–23] but the ability to encode nanoparticle interactions in a selective and reversible fashion in the specificity of the DNA sequence goes far beyond what is possible with ordinary atoms.[21,24]

Most experimental and computational studies[22,25–28] have focused on *spherical* nanoparticles that are functionalized with DNA. However, one can also combine the best of both worlds and combine *DNA-functionalization* with *anisotropic particle shapes*, such as Janus particles,[29] cuboctahedra, cubes and octahedra, as well as mixtures of cubic particles with different degrees of convexity and concavity.[30] By decorating these shape-anisotropic particles with a soft deformable shell of DNA ligands, an intricate competition arises between the optimal packing of these building blocks as determined by maximizing the system's entropy and the structure that is favored by the energetic interactions arising between DNA strands.[31] This intriguing interplay between energetic and entropic contributions to the self-assembly can be exploited not only to diversify the nanoparticle superlattice structures but also to control and direct their self-assembly.

In this paper, we focus on the effect of DNA hybridization on the self-assembly of cubic nanoparticles. The cube is a space-filling convex polyhedron consisting of 6 regular square faces and is considered to be one of the simplest anisotropic particle shapes. Simulation studies showed that hard cubes crystallize into simple cubic crystal phases with a surprisingly high vacancy concentration,[8,32] whereas truncated hard cubes stabilize deformed simple cubic crystal structures.[33,34] Rounded hard cubes form deformed simple cubic (or rhombohedral), deformed face-centered cubic (fcc), as well as plastic fcc phases.[35,36] Simple cubic, rhombohedral, and plastic crystal phases have indeed been observed in experiments on micrometer-sized silica cubes,[37,38] silver nanocubes,[39] and truncated metal-organic-framework particles.[40] The self-assembly of other structures can be obtained by complementing the excluded-volume interactions with enthalpic interactions. For instance, 1D structures with either face-to-face or edge-to-edge oriented cubes were obtained by grafting the particles with polymer or ligands;[41–43] linear chains, 2D square and honeycomb lattices[44,45] were found by preferential adsorption of a specific particle orientation at a fluid interface as well as by oriented attachment; and linear chains and square, honeycomb, and hexagonal lattices with edge-up, face-up, and vertex-up oriented cubes were assembled using capillary interactions.[46–49]

Additionally, grafting DNA ligands on the surface of cubic nanoparticles leads to *directional* DNA interactions as provided by the six facets of the cube.[50] O'Brien *et al.* investigated the self-assembly behavior of cubic nanoparticles using DNA linkers with self-complementary sticky ends so that particles can bind to all other particles in solution.[50] Using molecular dynamics simulations, these authors determined the range of DNA lengths and nanoparticle surface areas where the orientations of the individual cubes, and the crystallization behavior is predominately determined by the anisotropic particle shape and DNA shell. They found that for short DNA length and large nanoparticle surface area, the nanocubes self-assemble into a simple cubic (SC) crystal structure, but upon increasing the DNA length and decreasing the surface area, the system transitions to a body-centered tetragonal (BCT) and plastic BCT phase. In the case of two sets of nanocubes that are functionalized with complementary DNA, particles can only bind to particles of the opposite species. In the case of spheres, it was already observed that for one-component spherical DNA-functionalized nanoparticles with self-complementary sticky ends, the system self-assembles into a face-centered cubic (fcc) crystal phase, while body-centered cubic (bcc) phases (corresponding to cesium chloride (CsCl) phases if the two species are distinguished) were found in binary systems of spherical nanoparticles grafted with complementary sticky ends.[18] The case of binary mixtures of DNA-functionalized nanocubes with complementary DNA strands was investigated by Lu *et al.* in Ref. 51. They found that the cubes are tilted with respect to the lattice vectors for both the bcc and BCT phase, and they explained this unusual packing of nanocubes by the anisotropic particle shape and the preferential adsorption of the DNA ligands to regions of high curvature on the particle surface.

In this work, we study the self-assembly behavior of binary mixtures of nanocubes, which are grafted by *immobilized* complementary DNA strands, using extensive molecular dynamics (MD) simulations. We determine the self-assembled crystal structures of DNA-functionalized nanocubes as a function of DNA length, grafting density, and rigidity of the DNA, and we map out the corresponding phase diagrams. In addition, we measure the potential of mean force for DNA-functionalized nanocubes for varying rigidity of the DNA strands and DNA lengths. Finally, we show using free-energy calculations that longer and more flexible DNA strands can lead to a phase transformation from SC to the plastic BCT phase due to a gain in entropy arising from the orientational degrees of freedom of the nanocubes in the pBCT phase.

II. MODEL

To study the self-assembly behavior of DNA-functionalized nanocubes, we adopt the coarse-grained model for isotropic DNA-functionalized nanoparticles as introduced by Knorowski *et al.*[26] and Li *et al.*,[27,28] which we extend to investigate the shaped-induced crystallization of binary DNA-functionalized cubic gold nanoparticles (DNA-AuNPs). The coarse-grained model is schematically depicted in Fig. 1.

We model the surface of a cubic gold nanoparticle (AuNP) with edge length $L = 10$ nm as a rigid body consisting of a shell of beads. All the beads are constrained with respect to the center-of-mass of the rigid body, preventing the shape of the nanoparticle and the length of its sides from changing. Furthermore, we assume that there are no interactions between the beads on the surface. To investigate the effect of the rigidity of the DNA strands on the self-assembly, we graft the cubic core with either single-stranded DNA (ssDNA) or double-stranded DNA (dsDNA) with the dsDNA being more rigid than the ssDNA. The DNA chains are randomly tethered on the surface of the cube. Both the ssDNA and dsDNA chains consist of an anchor strand that attaches the DNA to the nanoparticle, a spacer strand, and a linker strand. The anchor strand is represented by a single-stranded (SS) DNA bead with a diameter of $\sigma_{SS} \approx$ 1 nm representing ~2 to 3 DNA bases. The spacer strand consists of either $n_{SS} \in [2, 12]$ single-stranded (SS) spacer (yellow) beads with a
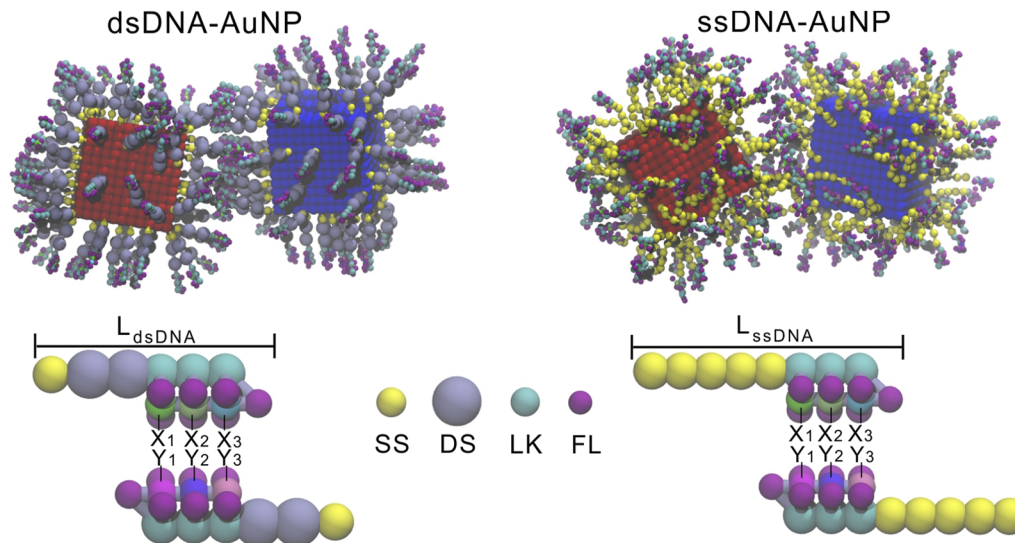
FIG. 1. Schematic picture of our coarse-grained model of a binary mixture of DNA-functionalized cubic nanoparticles and examples of hybridizations between two gold (Au) nanocubes (NP) with complementary double-stranded DNA (dsDNA) (left) or single-stranded DNA (ssDNA) (right). A DNA strand consists of spacer beads representing double-stranded (DS) or single-stranded (SS) DNA, linker beads (LK), flanking beads (FL), and sticky-end beads (X_1, X_2, X_3 and Y_1, Y_2, Y_3). The total length of the dsDNA and ssDNA strand is denoted by L_{dsDNA} and L_{ssDNA}, respectively.

diameter of $\sigma_{SS} \approx 1$ nm or $n_{DS} \in [1,6]$ double-stranded (DS) spacer (gray) beads with a diameter of $\sigma_{DS} \approx 2$ nm representing ~5 DNA base-pairs. We choose $\sigma = \sigma_{DS}$ as our unit of length. Finally, the linker strand consists of 3 linker (LK) beads, which are decorated by sticky-end (SE) beads and flanking (FL) beads. The SE beads are positioned on top of the LK beads. The SE beads X_1, X_2, X_3 can hybridize complementary base pairs Y_1, Y_2, Y_3, respectively, via a truncated and shifted Lennard-Jones interaction,

$$U_{XY}(r) = \begin{cases} 4\varepsilon_{XY}\left[\left(\dfrac{\sigma_{XY}}{r}\right)^{12} - \left(\dfrac{\sigma_{XY}}{r}\right)^{6}\right] - U_{XY}^{\text{shift}} & \text{for } r \leq r_{cut}, \\ 0 & \text{for } r > r_{cut}, \end{cases} \quad (1)$$

where $\sigma_{XY} = 0.6\sigma$ is the interactive distance between the SE beads, r is the distance between the SE beads, $r_{cut} = 2.5\sigma$ is the cut-off distance, and $U_{XY}^{\text{shift}} = 4\varepsilon_{XY}\left((\sigma_{XY}/r_{cut})^{12} - (\sigma_{XY}/r_{cut})^{6}\right)$. We set $\varepsilon_{XY} = 4\varepsilon$, with ε being our unit of energy to represent the attractive strength of the non-covalent bonds between complementary base pairs.

To make the hybridization (formation of hydrogen bonds) directional and to prevent that more than two SE beads form a bond, the SE beads are flanked by FL beads. All the beads different from the SE beads interact via a purely repulsive Weeks–Chandler–Andersen potential,

$$U_{\alpha\beta}(r) = \begin{cases} 4\varepsilon\left[\left(\dfrac{\sigma_{\alpha\beta}}{r}\right)^{12} - \left(\dfrac{\sigma_{\alpha\beta}}{r}\right)^{6}\right] + \varepsilon & \text{for } r \leq 2^{1/6}\sigma_{\alpha\beta}, \\ 0 & \text{for } r > 2^{1/6}\sigma_{\alpha\beta}, \end{cases} \quad (2)$$

with α, β corresponding to either LK, FL, SS, or DS beads. All interactive distances $\sigma_{\alpha\beta}$ are listed in Table I. The DNA coarse-grained beads are connected by covalent bonds via a harmonic spring potential, $U_{\text{bond}}(r) = (1/2)k_s(r - r_0)^2$, where $k_s = 220\varepsilon/\sigma^2$ is the spring constant and $r_0 = 0.84\sigma_{\alpha\beta}$ is the native spring length. The harmonic angle potential $U_{\text{angle}}(\theta) = (1/2)k_\theta(\theta - \theta_0)^2$ is used to enforce the rigidity of the DNA and to align neighboring sticky-end (SE) and their flanking (FL) beads, where θ represents the angle between three consecutive beads. For dsDNA strands, we chose $k_\theta = 20\varepsilon/\text{rad}^2$ based on Ref. 27. For the ssDNA strands, the value of k_θ should be relatively small. We therefore set k_θ to a relatively small value, i.e., $5\ \varepsilon/\text{rad}^2$, for which ssDNA shows random coil behavior. The equilibrium angle is $\theta_0 = \pi$. To keep the LK and FL beads in their position, we

TABLE I. Interactive distances $\sigma_{\alpha\beta}/\sigma$ with $\sigma = 2$ nm our unit of length.

$\alpha\beta$	SS	DS	LK	FL	X_1	X_2	X_3	Y_1	Y_2	Y_3
SS	0.5	0.75	0.5	0.4	0.4	0.4	0.4	0.4	0.4	0.4
DS	$\cdots$	1.0	0.75	0.5	0.5	0.5	0.5	0.5	0.5	0.5
LK	$\cdots$	$\cdots$	0.5	0.4	0.6	0.6	0.6	0.6	0.6	0.6
FL	$\cdots$	$\cdots$	$\cdots$	0.4	0.43	0.43	0.43	0.43	0.43	0.43
X_1	$\cdots$	$\cdots$	$\cdots$	$\cdots$	1.0	0.3	0.3	0.6	0.3	0.3
X_2	$\cdots$	$\cdots$	$\cdots$	$\cdots$	0.3	1.0	0.3	0.3	0.6	0.3
X_3	$\cdots$	$\cdots$	$\cdots$	$\cdots$	0.3	0.3	1.0	0.3	0.3	0.6
Y_1	$\cdots$	$\cdots$	$\cdots$	$\cdots$	$\cdots$	$\cdots$	$\cdots$	1.0	0.3	0.3
Y_2	$\cdots$	$\cdots$	$\cdots$	$\cdots$	$\cdots$	$\cdots$	$\cdots$	0.3	1.0	0.3
Y_3	$\cdots$	$\cdots$	$\cdots$	$\cdots$	$\cdots$	$\cdots$	$\cdots$	0.3	0.3	1.0

employ $k_\theta = 100\varepsilon/\text{rad}^2$ for the FL–LK–FL angle, $k_\theta = 120\varepsilon/\text{rad}^2$ for DS–LK–SE and SS–LK-SE angle, and $k_\theta = 50\varepsilon/\text{rad}^2$ for SE–SE–FL angle.

To achieve effective crystallization, the thermally active hybridization events between sticky ends (breaking and reforming of hydrogen bonds) is the key factor. We find that a temperature $k_B T/\varepsilon \in [1.4, 1.8]$ yields spontaneous crystallization. We perform MD simulations in the *NVT* ensemble with the temperature controlled by a Nosé–Hoover thermostat using the HOOMD-blue package.[52–54]

III. RESULTS

We study the self-assembly of DNA-functionalized nanocubes as a function of DNA length L_{ssDNA} and L_{dsDNA} ranging from 4.5 to 14.5 nm and grafting density ρ ranging from 0.050 to 0.150 strands/nm^2. The grafting density is defined as $\rho = N_{DNA}/S_{cube}$, where N_{DNA} is the total number of DNA strands and S_{cube} is the surface area of the nanoparticle core. We use a fluid-like configuration in a cubic simulation box as the initial configuration and randomize the system at high temperature $k_B T/\varepsilon = 2$. We employ periodic boundary conditions. Subsequently, we run the simulations at the temperature of interest for about 2.0×10^8 time steps to reach the maximum DNA hybridization and to self-assemble the nanocubes in various structures. The size of the time step is kept constant at $\delta t = 0.001\tau$, where $\tau = \sqrt{((m\sigma^2)/\varepsilon)}$.

A. Crystal structures

In Figs. 2(a)–2(c) (Multimedia view), we present typical configurations obtained from our simulations on the self-assembly of dsDNA-AuNPs. To identify the crystal structures, we not only use a visual inspection of the configurations, but we also determine the diffraction patterns in the *yz*- and *xy*-plane. The diffraction patterns in Fig. 2(d) confirm that the dsDNA-AuNPs with $L_{\text{dsDNA}} = 6.5$ nm assemble into a simple cubic (SC) phase with compositional and orientational order, as shown by the configuration in Fig. 2(a) (Multimedia view). The situation changes if we consider dsDNA-AuNPs with $L_{\text{dsDNA}} = 10.5$ nm for which we find that the NPs self-assemble into a superlattice with a structure that is different from the SC phase and with orientational disorder and compositional order [see Fig. 2(b) (Multimedia view)]. By examining the diffraction pattern in Fig. 2(e), we find that the lattice constants $D_x = D_y \neq D_z$, indicating a plastic body-centered tetragonal pBCT crystal. Upon further increasing the dsDNA length to $L_{\text{dsDNA}} = 14.5$ nm, the system eventually assembles into a compositional disordered pBCT (d-pBCT) lattice [Fig. 2(c), Multimedia view].

In addition, we investigate the effect of rigidity of the DNA on the self-assembled structures. To this end, we studied the self-assembly of ssDNA-AuNPs using the same range of DNA lengths. The ssDNA is less rigid than the dsDNA. As shown in Figs. 3(a)–3(c) (Multimedia view), we find the same crystal structures, SC, pBCT, and d-pBCT phase, as we already observed for the self-assembly of dsDNA-AuNPs. To obtain further insight in the orientations of the cubes in the pBCT phase, we show side views of the simulation configurations in Fig. 4 for nanoparticles decorated with dsDNA and ssDNA. We clearly observe that the dsDNA strands are more

rigid than the ssDNA strands. In addition, we find that the lattice spacings of the cubes are equal in the *x*- and *y*-direction and that the lattice spacings in the *z*-direction are substantially larger, which is consistent with the corresponding diffraction patterns of pBCT.

B. Phase diagrams and hybridization

In order to investigate the effect of directional DNA interactions on the self-assembly of cubic nanoparticles, we systematically study the self-assembly of dsDNA-AuNPs as a function of DNA length L_{dsDNA} and grafting density ρ at temperature $k_B T/\varepsilon = 1.6$. We show the resulting phase diagrams for dsDNA-AuNPs in the $L_{\text{dsDNA}} - \rho$ plane in Fig. 5(a). For each state point in the phase diagram, we simulate five independent runs. The phase diagram displays a disordered fluid, SC, pBCT, and d-pBCT phases. For sufficiently long DNA length and sufficiently low grafting density, the NPs present a disordered fluid phase, whereas the NPs self-assemble into a SC phase for sufficiently short DNA length and sufficiently high grafting density. The pBCT phase is formed for intermediate grafting densities, i.e., $\rho \in [0.05, 0.100]$ strands/nm^2, and intermediate DNA lengths i.e., $L_{\text{dsDNA}} \in [4, 12]$ nm. Finally, the NPs self-assemble into a compositionally and orientationally disordered BCT phase for sufficiently long DNA lengths. The compositional disorder originates from kinetically trapped compositional defects in the pBCT lattice.[55,56] To study the effect of rigidity of the DNA strands on the phase behavior, we also determine the phase diagram of ssDNA-AuNPs as a function of grafting density ρ and length L_{ssDNA} of the ssDNA. We find that higher stiffness of the DNA chains results in a higher propensity of ordered crystalline structures, which is consistent with recent work on the self-assembly of polymer-grafted nanoparticles.[57]

We now take a closer look at the hybridization of the DNA linkers and the crystallization process. To this end, we study the effect of DNA length, grafting density, and temperature on the percentage of hybridized DNA linkers $p(H)$ during the crystallization process. We define a hybridization event when each sticky-end bead on a DNA strand forms a non-covalent bond with its complementary sticky-end bead, i.e., when the two beads are within a distance of $1.5\sigma_{\alpha\beta}$. We show the percentage of hybridizations $p(H)$ as a function of time for dsDNA-AuNPs and ssDNA-AuNPs for varying DNA lengths in Figs. 6(a) and 6(b) and for varying grafting densities in Figs. 6(c) and 6(d). We find that in all cases, $p(H)$ reaches a constant value within $2 \times 10^7 \delta t$. In addition, we find that the percentage of hybridizations $p(H)$ decreases with DNA length and increases with grafting density. We thus find that both the DNA length and the grafting density play a key role in the DNA hybridization and the crystallization process. The decrease in $p(H)$ as the DNA length increases can be explained by a reduction in the local concentration of sticky ends. This effect can be attributed to the increased volume accessible to sticky ends as longer DNA strands are used, which leads to an increase in configurational entropy of the DNA ligands and repulsion between DNA-functionalized nanocubes[58] and, consequently, resulting in a decrease in $p(H)$. We now study the effect of temperature on the hybridization process. We first make a few observations. We find that at high grafting density and low temperature, the number of hybridized DNA linkers can be so high that the system gets kinetically trapped, while at low grafting density and
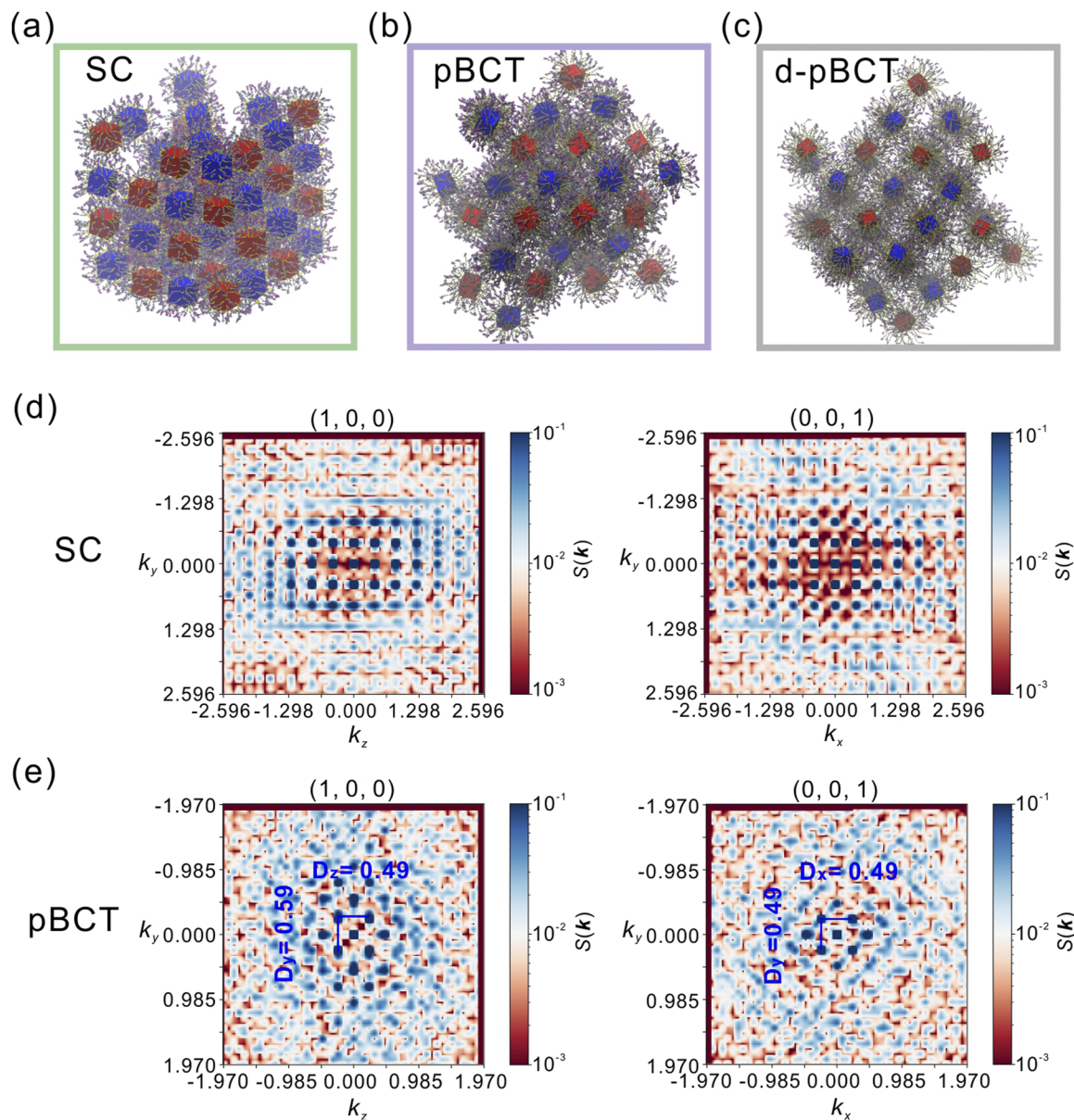
FIG. 2. Representative configurations of double-stranded DNA-functionalized gold nanocubes (dsDNA-AuNPs) with a grafting density $\rho = 0.15$ strands/nm^2 obtained from MD simulations at a temperature $k_B T / \varepsilon = 1.8$: (a) simple cubic (SC) crystal phase of NPs with a DNA length $L_{dsDNA} = 6.5$ nm (Multimedia available online), (b) plastic body-centered tetragonal (pBCT) phase of NPs with $L_{dsDNA} = 10.5$ nm (Multimedia available online), and (c) compositionally disordered plastic body-centered tetragonal (d-pBCT) of NPs with $L_{dsDNA} = 14.5$ nm (right) (Multimedia available online). [(d) and (e)] Diffraction patterns of the (100) plane (xz plane) or (001) plane (xy plane) of the corresponding SC and pBCT phase.

high temperature, the number of hybridization events is too low for the formation of ordered structures. We therefore adjust the temperature to find the most optimal temperature for crystallization. In Figs. 6(e) and 6(f), we exemplarily show the percentage of hybridization $p(H)$ for the optimal temperature for crystallization for varying grafting densities and DNA length $L_{dsDNA} = L_{ssDNA} = 4.5$ nm. By optimizing the temperature for the crystallization process of DNA-functionalized gold nanocubes for a typical grafting density,

we find that the region for the formation of ordered crystalline structures, i.e., SC and pBCT, significantly broadens, as shown in Fig. 5(b).

C. Potential of mean force

Additionally, we observe that as the length of DNA increases for a given particle size, the propensity of forming BCT crystal
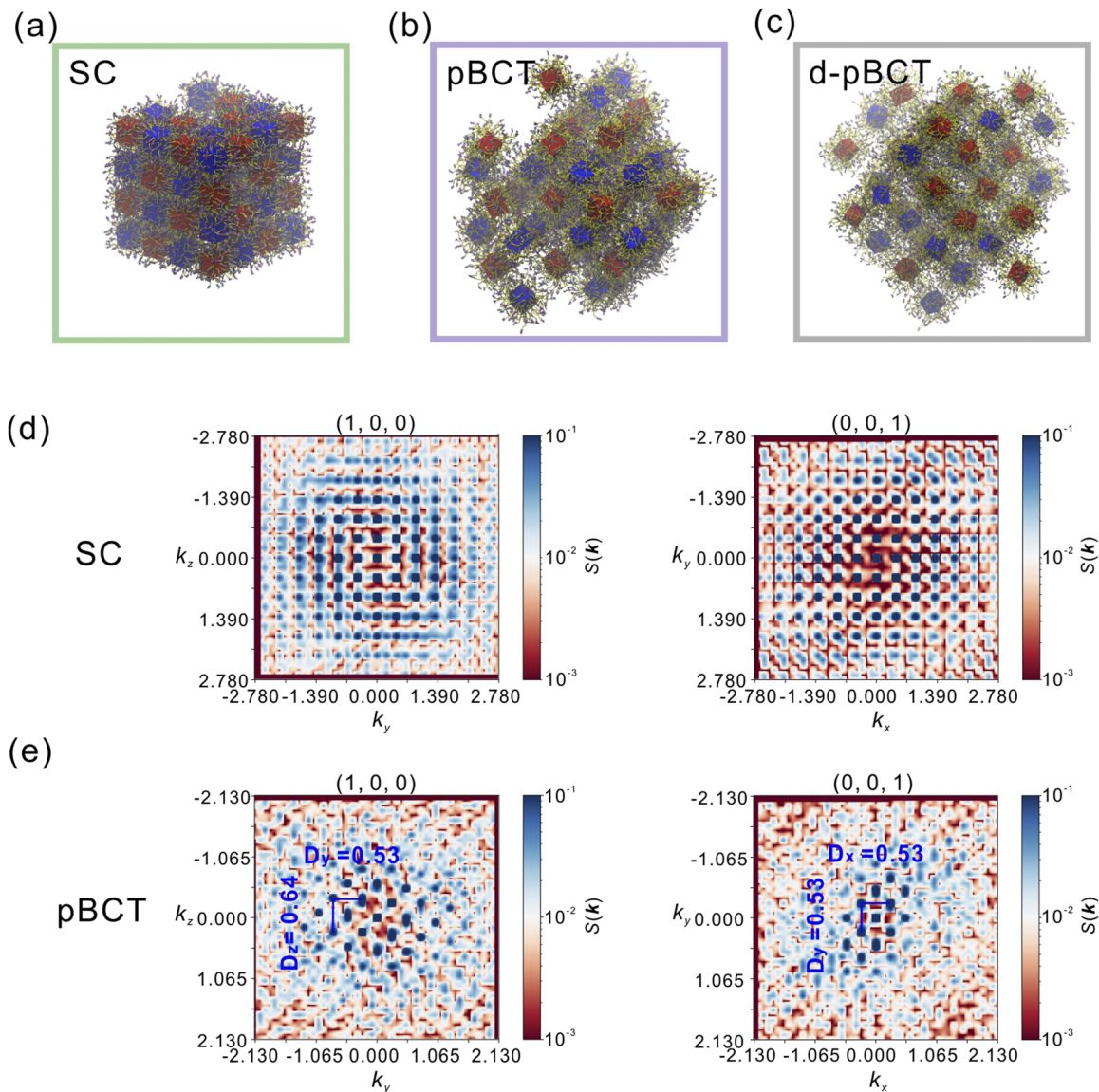
FIG. 3. Representative configurations of single-stranded DNA-functionalized gold nanocubes (ssDNA-AuNPs) with a grafting density $\rho = 0.15$ strands/nm^2 obtained from MD simulations at a temperature $k_B T/\varepsilon = 1.8$: (a) simple cubic (SC) crystal phase of NPs with a DNA length $L_{ssDNA} = 4.5$ nm (Multimedia available online), (b) plastic body-centered tetragonal (pBCT) phase of NPs with $L_{ssDNA} = 10.5$ nm (middle) (Multimedia available online), and (c) compositionally disordered plastic body-centered tetragonal (d-pBCT) of NPs with $L_{ssDNA} = 14.5$ nm (right) (Multimedia available online). [(d) and (e)] Diffraction patterns of the (100) plane (xz plane) or (001) plane (xy plane) of the corresponding SC and pBCT phase.

structures with compositional disorder increases. In order to shed light on the effect of DNA length on the self-assembly process, we measure the potential of mean force between two dsDNA-AuNPs or ssDNA-AuNPs with varying DNA lengths. We use constraint bias MD simulations to keep the center-of-mass distance R_{ij} frozen between nanoparticle i and j and measure the mean force,

$$F_m(R_{ij}) = \frac{1}{2}\langle (\mathbf{F}_i - \mathbf{F}_j) \cdot \hat{\mathbf{R}}_{ij} \rangle, \qquad (3)$$

as the average force along the center-of-mass distance vector $\hat{\mathbf{R}}_{ij}$ and with $\mathbf{F}_i$ and $\mathbf{F}_j$ being the total force acting on nanoparticle i and j, respectively. The angular brackets denote an ensemble average in the canonical ensemble. We run the simulations for $3 \times 10^7 \delta t$ in a periodic box and use the last $2 \times 10^7 \delta t$ for sampling. The potential of mean force $\Phi(R)$ is then computed by

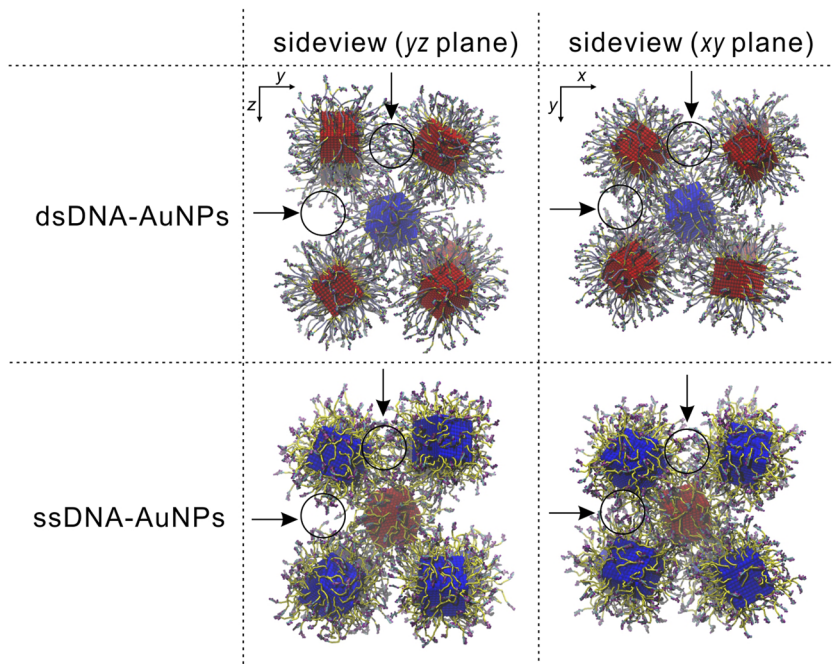$$\Phi(R) = \int_R^\infty F_m(R_{ij}) dR_{ij}. \qquad (4)$$

FIG. 4. Representative configurations from two different viewpoints of the plastic body-centered tetragonal (pBCT) phase of (top) double-stranded and (bottom) single-stranded DNA-functionalized gold nanocubes (dsDNA-AuNPs and ssDNA-AuNPs, respectively) with a grafting density $\rho = 0.15$ strands/nm^2 obtained from MD simulations.

We plot the potential of mean force $\Phi(R)$ of dsDNA-AuNPs and ssDNA-AuNPs for varying DNA lengths in Fig. 7. We clearly observe that the attractive well of $\Phi(R)$ becomes less pronounced and shifts to larger distances upon increasing the DNA length, which may explain the compositional disorder seen in the BCT crystal phases. In addition, we find that the potential of mean force $\Phi(R)$ is less attractive for ssDNA-AuNPs than for dsDNA-AuNPs.

D. SC-pBCT phase transformation

To confirm the thermodynamic stability of pBCT of dsDNA-AuNPs with a DNA length of $L_{\text{dsDNA}} = 10.5$ nm, we perform an MD simulation for $2 \times 10^8 \delta t$ in which we start with an orientationally ordered and equilibrated SC crystal phase. To monitor the transformation process, we examine the translational and rotational dynamics of the NPs by calculating the root mean square displacement $\text{RMSD}(t) = \sqrt{\langle |\mathbf{R}(t) - \mathbf{R}(0)|^2 \rangle}$ and the second-order orientational order parameter $S(t) = \langle (3\cos^2 \theta(t) - 1)/2 \rangle$, where $\mathbf{R}$ denotes the center-of-mass position of a nanocube, $\theta(t)$ denotes its orientation with respect to a director $\hat{\alpha}$, and the angular brackets denote an ensemble average. The second-order orientational order parameter $S(t)$ measures the alignment of particles along $\hat{\alpha}$, where $S(t) = 1$ represents perfect alignment and $S(t) = 0$ denotes completely random orientational order. We plot the $\text{RMSD}(t)$ and $S(t)$ in Fig. 8(a), along with representative configurations showing the spontaneous transformation from the SC to the pBCT phase in Fig. 8(b), indicating that the pBCT phase is indeed the stable structure for dsDNA-AuNPs with long DNA strands, i.e., $L_{\text{dsDNA}} = 10.5$ nm. The percentage of hybridizations $p(H)$ as shown in Fig. 8(c) is also measured over time. The transformation process can be divided into two parts. In the initial part, which occurs over a

short period of time ($\sim 1.9 \times 10^7 \delta t$), the root mean square displacement $\text{RMSD}(t)$ increases and the orientational order $S(t)$ decreases, until it stabilizes after $\sim 1.9 \times 10^7 \delta t$. In addition, the percentage of hybridizations $p(H)$ immediately decreases and remains stable at about 0.07, where the hybridization strength is still sufficiently strong to stabilize the superlattice structure of dsDNA-AuNPs.

E. Plastic crystal behavior

Plastic crystals (rotator phases) are characterized by long-ranged positional order and short-ranged orientation order. To investigate the effect of length, grafting density, and rigidity of the DNA on the orientational order of the nanoparticles in the plastic crystal phases, we measure the orientation correlation function $g_4(R)$,

$$g_4(R) = \frac{3}{14} \left\langle 35 \left[\mathbf{u}_{i\alpha}(0) \cdot \mathbf{u}_{j\alpha}(R) \right]^4 - 30 \left[\mathbf{u}_{i\alpha}(0) \cdot \mathbf{u}_{j\alpha}(R) \right]^2 + 3 \right\rangle, \quad (5)$$

where the angular brackets denote an ensemble average over all the particle axes $\alpha = 1, 2, 3$ and particle pairs i and j.[34,35] We refer the reader to Ref. 59 for more details. In Fig. 9, we plot the results for dsDNA-AuNPs and ssDNA-AuNPs with varying DNA lengths in the SC and pBCT phase. By increasing the length of the DNA, the cubic particle shape may become completely masked and the orientation correlations may vanish, resulting in the formation of a plastic crystal phase [Fig. 9(c)]. Additionally, the orientation correlations may vanish when the grafting density decreases. Furthermore, we observe that in the case of more flexible DNA, i.e., ssDNA-AuNPs, the orientation correlations are less pronounced, which is
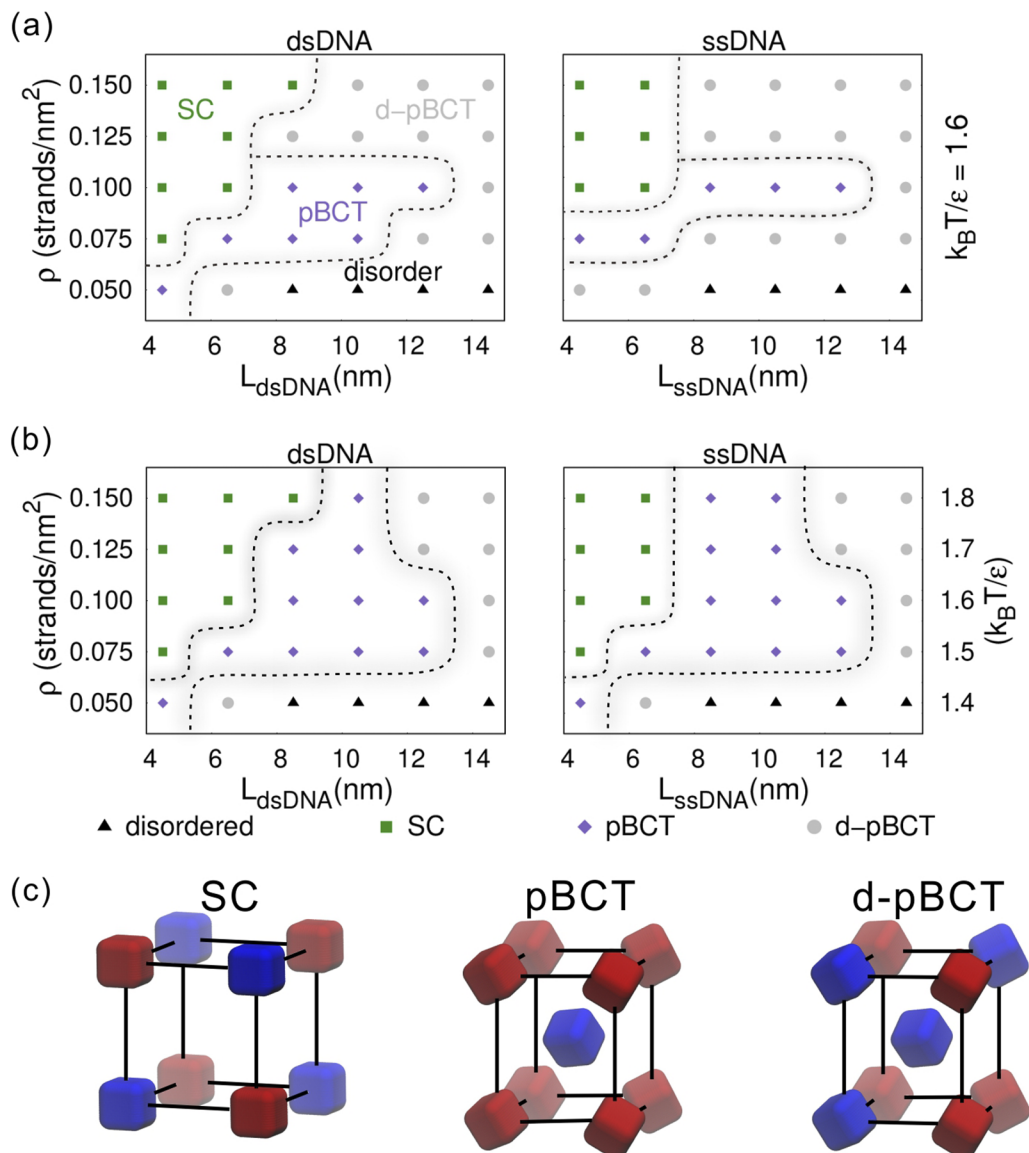
FIG. 5. Phase diagrams of (left) double-stranded DNA-functionalized gold nanocubes (dsDNA-AuNPs) and (right) single-stranded DNA-functionalized gold nanocubes (ssDNA-AuNPs) (a) in the DNA length (L_{dsDNA} or L_{ssDNA}) vs grafting density ρ representation at a temperature $k_B T/\varepsilon = 1.6$ and (b) at the optimal temperature for self-assembly ranging from $k_B T/\varepsilon \in [1.4, 1.8]$ (right axis) depending on ρ (left axis). The phase diagrams display a disordered fluid phase (black triangle), simple cubic (SC) crystal phase (green square), plastic body-centered cubic (pBCT) crystal phase (purple diamond), and a compositionally disordered pBCT (d-pBCT) phase (gray circle). Black dashed lines indicate approximate phase boundaries. (c) Schematic representation of the SC, pBCT, and d-pBCT structures.

consistent with the potential of mean force $\Phi(R)$ being less attractive for ssDNA-AuNPs than for dsDNA-AuNPs, as shown in Fig. 7.

These observations suggest that the spatial distribution of hybridized DNA linkers plays an important role in driving the phase transformation from the SC phase to the pBCT phase. To investigate this, we measure the averaged percentage of hybridized DNA linkers on the edges of the two cubes, the faces of the two cubes, and on the face of one cube and the edge of the other cube. We first differentiate all the DNA strands into face or edge (including the corners) linkers and then calculate the percentage of face-edge hybridizations between nanoparticle A and B as $2N_{face-edge}/(N_{face}^A + N_{edge}^A + N_{face}^B + N_{edge}^B)$, where $N_{face-edge}$ denotes the number of DNA strands on the edge (face) of nanoparticle A that are hybridized with DNA strands on the face (edge) of nanoparticle B and $N_{face(edge)}^I$ is the number of DNA strands on the face (edge) of nanoparticle $I = A, B$. The percentage of edge–edge
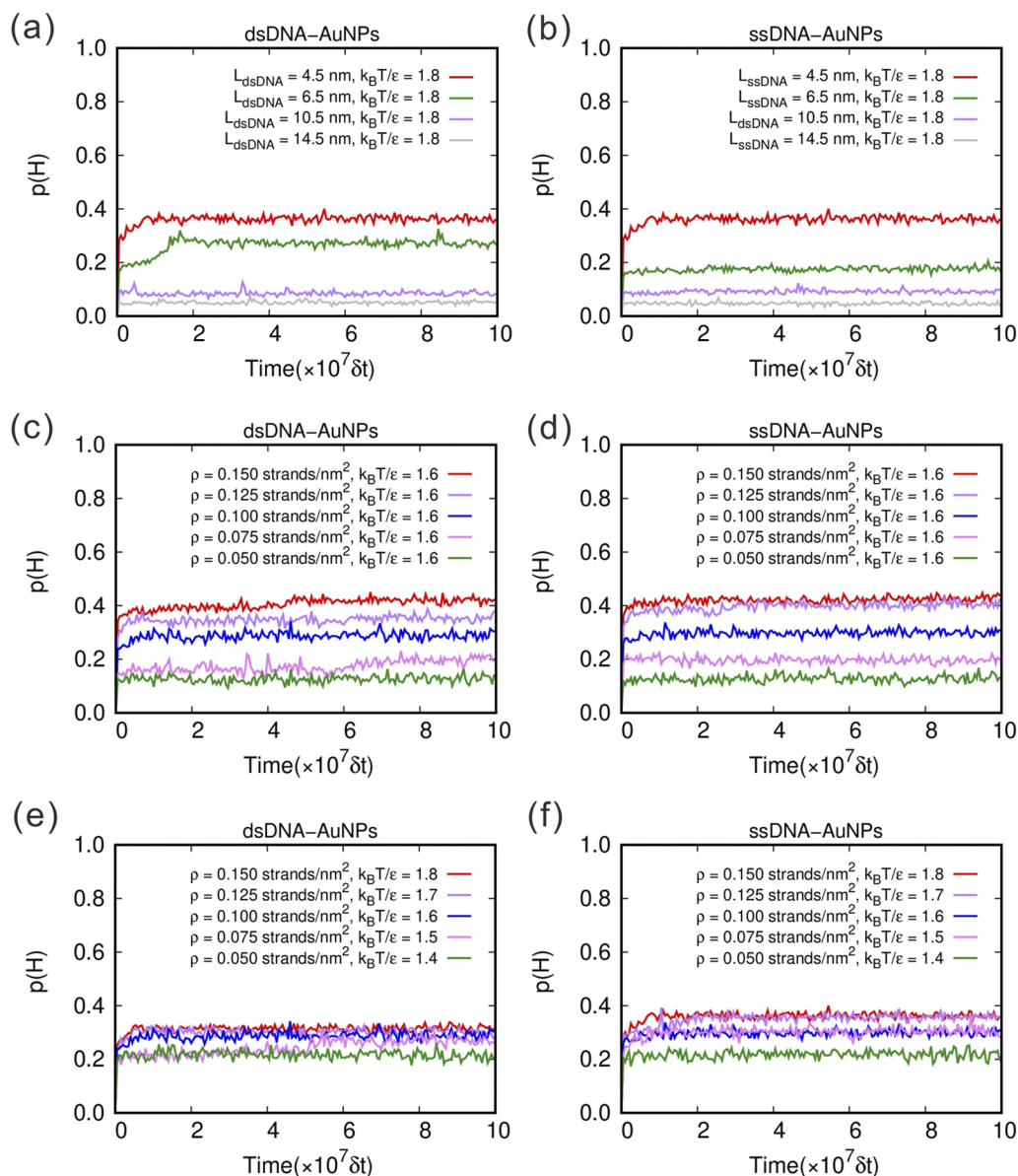
FIG. 6. Percentage of hybridization of DNA linkers $p(H)$ as a function of time for (a) double-stranded DNA-functionalized gold nanocubes (dsDNA-AuNPs) and (b) single-stranded DNA-functionalized gold nanocubes (ssDNA-AuNP) with grafting density $\rho = 0.150$ strands/nm^2 at temperature $k_B T/\varepsilon = 1.8$ for varying DNA lengths L_{dsDNA} and L_{ssDNA}, respectively, as labeled, for (c) dsDNA-AuNPs and (d) ssDNA-AuNPs with DNA length $L_{dsDNA} = L_{ssDNA} = 4.5$ nm at temperature $k_B T/\varepsilon = 1.6$ for varying grafting densities ρ as labeled, and finally, the percentage of hybridization $p(H)$ for (e) dsDNA-AuNPs and (f) ssDNA-AuNPs with DNA length $L_{dsDNA} = L_{ssDNA} = 4.5$ nm and varying grafting density as labeled for the optimal temperature for crystallization.

and face–face hybridizations between nanoparticle A and B are defined similarly. We plot the results in Figs. 10(b)–10(d). We find from Figs. 10(b) and 10(c) that for high grafting densities $\rho = 0.150$ strands/nm^2, the SC crystal phase is stabilized by face–face hybridizations, whereas the pBCT crystal has a preference for edge–edge hybridizations. However, as the DNA grafting density decreases to $\rho = 0.100$ strands/nm^2, the preference for face–face

and edge–edge hybridizations becomes similar to that for edge–face hybridizations for the SC phase, as shown in Fig. 10(d), reducing the orientational order of the cubes. In Fig. 11, we show the percentage of edge–edge, face–face, and edge–face hybridizations between ssDNA-AuNPs. We find that the SC crystal phase is stabilized by edge–edge hybridizations, as shown in Figs. 11(a) and 11(c) in contrast to dsDNA-AuNPs, which show a preference for face–face
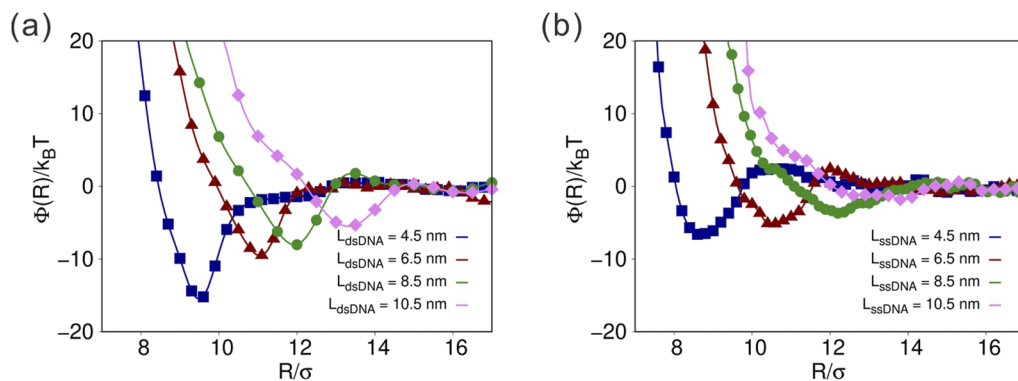
FIG. 7. Potential of mean force $\Phi(R)$ as a function of the center-of-mass distance R between dsDNA-AuNPs (a) and ssDNA-AuNPs (b) with a grafting density $\rho = 0.100$ strands/nm^2 and varying DNA lengths as labeled at a temperature $k_B T/\varepsilon = 1.6$.
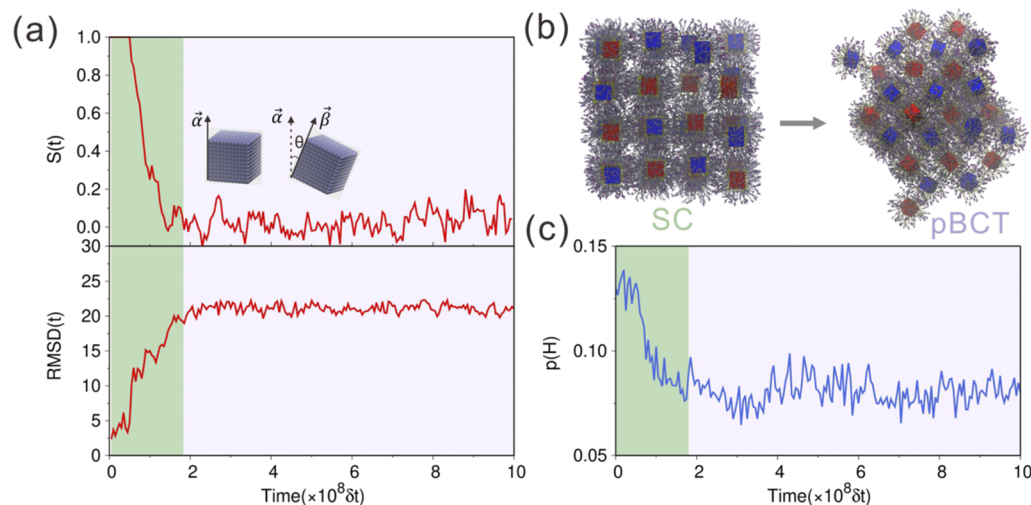

FIG. 8. The SC-pBCT phase transformation of dsDNA-AuNPs with $L_{dsDNA} = 10.5$ nm and $\rho = 0.150$ strands/nm^2. (a) Second-order orientational order parameter $S(t)$ (top) and root mean square displacement, RMSD (bottom), as a function of time when a predetermined SC configuration of dsDNA-AuNPs at $k_B T/\varepsilon = 1.8$. (b) Representative structures from the initial stage, i.e., the SC phase, to the final stage, i.e., the pBCT phase. The inset diagram illustrates the definition of θ. The green background indicates the initial part of the phase transformation. (c) Percentage of hybridization $p(H)$ as a function of time when the SC structure transform to the pBCT structure.

hybridizations in Fig. 10(b). The reduced face–face contact indicates weaker face–face interactions, leading to less orientational order of the cubes in the SC phase of ssDNA-AuNPs.

F. Free-energy calculations

Our results show that the phase transformation of a binary mixture of DNA-functionalized nanocubes from a SC to pBCT crystal structure is influenced by several factors, such as the length of the DNA strands, the grafting density, and the rigidity of the DNA strands. In addition, we expect that the transition from the SC to the pBCT phase is driven by an increase in entropy or number of microstates of the DNA.[50,60] To examine this in more detail, we selected four dsDNA-AuNPs systems with the same grafting density $\rho = 0.150$ strands/nm^2 but with different dsDNA lengths $L_{dsDNA} = 4.5, 6.5, 8.5,$ and 10.5 nm. Although it is not possible to calculate the entropy directly, we can estimate it by decomposing the free energy difference $\Delta F = \Delta U - T\Delta S$ into the internal energy ΔU and the entropy contribution $-T\Delta S$. To determine the stable superlattice structure of the dsDNA-AuNPs for different values of the DNA lengths, we employ the lattice-coupling expansion method[61,62] to calculate the free-energy differences between pBCT and SC superlattice structures.

The calculations are carried out in two stages using the azplugins software.[63] In the first stage, we introduce a harmonic interaction with a spring constant of $k = 60\varepsilon/\sigma^2$ between the center of each nanoparticle core and its equilibrium lattice site. To account for the orientational degrees of freedom of the particles, an
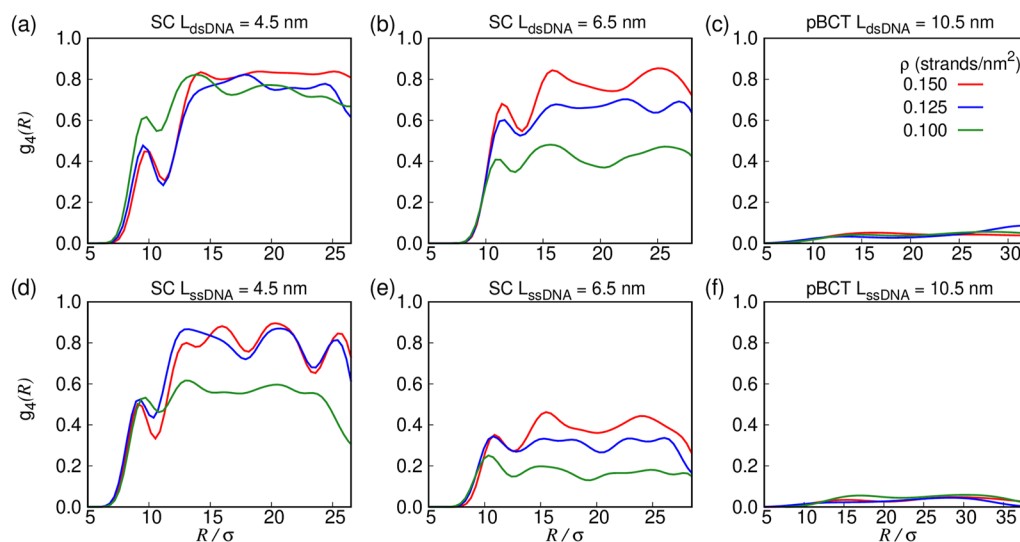
FIG. 9. Orientation correlation function $g_4(R)$ for the simple cubic (SC) crystal and plastic body-centered tetragonal (pBCT) phase formed by dsDNA-AuNPs with L_{dsDNA} = 4.5 nm (a), 6.5 nm (b), and 10 nm (c) or ssDNA-AuNPs with L_{ssDNA} = 4.5 nm (d), 6.5 nm (e), and 10.5 nm (f) as a function of the radial distance R scaled by the reduced unit σ. The investigated systems are at three different grafting density, i.e., 0.001, 0.125, and 0.150 strands/nm^2.
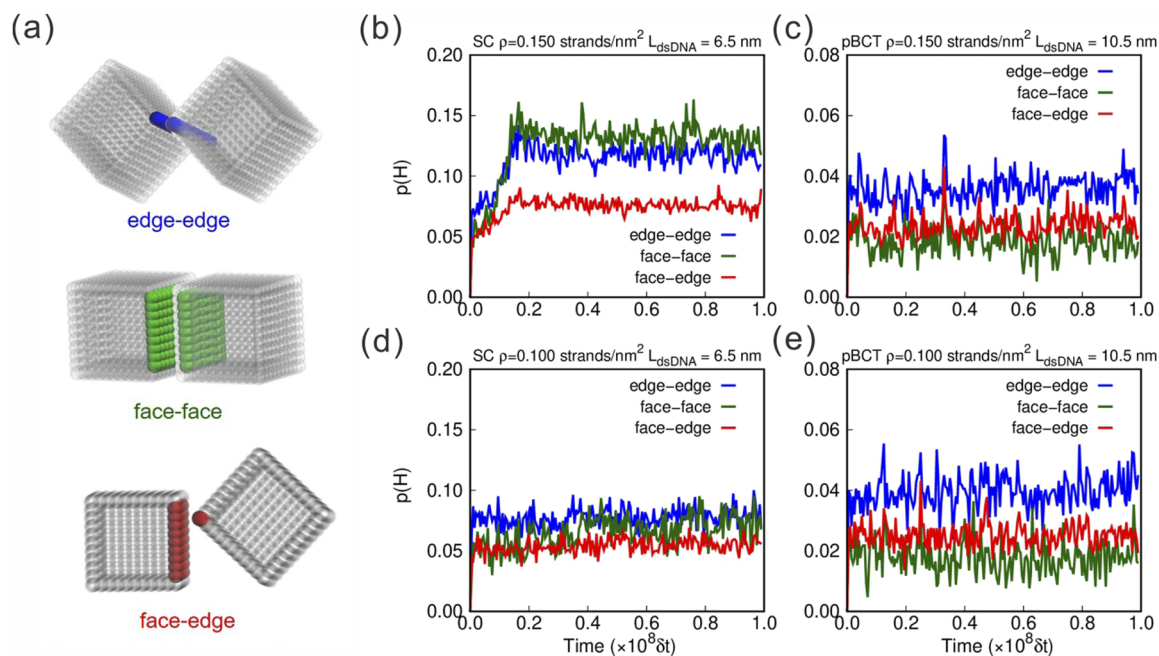

FIG. 10. (a) Schematic illustration of edge–edge, face–face, and edge–face DNA hybridizations. Percentage of edge–edge, face–face, and edge–face DNA hybridizations as a function of time for (b) a SC phase of dsDNA-AuNPs with a grafting density ρ = 0.150 strands/nm^2 and DNA length L_{dsDNA} = 6.5 nm, (c) a pBCT phase of dsDNA-AuNPs with a grafting density ρ = 0.150 strands/nm^2 and DNA length L_{dsDNA} = 10.5 nm, (d) a SC phase of dsDNA-AuNPs with a grafting density ρ = 0.100 strands/nm^2 and DNA length L_{dsDNA} = 6.5 nm, and (e) a pBCT phase of dsDNA-AuNPs with a grafting density ρ = 0.100 strands/nm^2 and DNA length L_{dsDNA} = 10.5 nm.
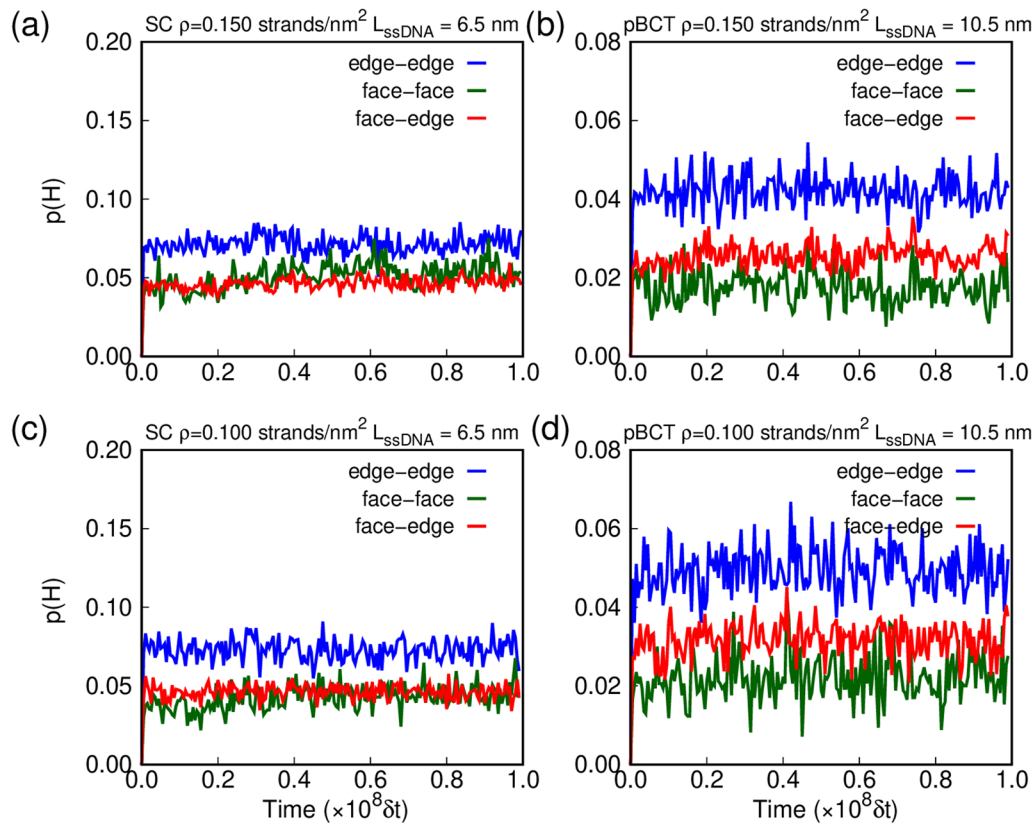
FIG. 11. Percentage of edge–edge, face–face, and edge–face DNA hybridizations as a function of time for (a) a SC phase of ssDNA-AuNPs with a grafting density $\rho = 0.150$ strands/nm^2 and DNA length $L_{ssDNA} = 6.5$ nm, (b) a pBCT phase of ssDNA-AuNPs with a grafting density $\rho = 0.150$ strands/nm^2 and DNA length $L_{ssDNA} = 10.5$ nm, (c) a SC phase of ssDNA-AuNPs with a grafting density $\rho = 0.100$ strands/nm^2 and DNA length $L_{ssDNA} = 6.5$ nm, and (e) a pBCT phase of ssDNA-AuNPs with a grafting density $\rho = 0.100$ strands/nm^2 and DNA length $L_{ssDNA} = 10.5$ nm.

independent coupling force with a spring constant of $k_o = 5000\varepsilon/\sigma^2$ is also imposed on each nanoparticle core to constrain its orientation. The simulations are performed in the NVT ensemble for a series of systems with different values of spring constants λk, where λ varies from 0 to 1 in increments of 0.05. We run each simulation with a fixed value of λ for 4.0×10^6 time steps, and the last 2.0×10^6 steps of the trajectory are used for sampling. The free-energy change ΔF_{spring} due to the spring coupling is calculated using thermodynamic integration,

$$\Delta F_{spring} = \int_0^1 d\lambda \left\langle \sum_{i=1}^N \frac{k}{2} (\mathbf{R}_i - \mathbf{R}_{i,0})^2 \right\rangle_\lambda, \quad (6)$$

where N denotes the number of particles, $\mathbf{R}_i$ is the center-of-mass position of nanoparticle i, $\mathbf{R}_{i,0}$ is the spring anchor points, i.e., the ideal lattice positions, and $\langle \cdots \rangle_\lambda$ denotes an ensemble average at a fixed value of λ.

In the second stage, the lattice-coupled solid is gradually expanded by scaling the positions of the spring anchor points with a linear expansion parameter γ, i.e., $\mathbf{R}_{i,0} \rightarrow \gamma \mathbf{R}_{i,0}$. The superlattice is expanded until the DNA-coated nanoparticles do not interact with

each other. The lattice expansion was performed in a series of values ranging from 1.000 to 1.40 with increments of 0.002 up to 1.01, 0.01 up to 1.07, 0.02 up to 1.19, and 0.03 up to 1.40. We run each simulation for at least 6.0×10^6 time steps, and the last 2.0×10^6 steps of the trajectory are used for sampling. The free-energy difference $\Delta F_{expansion}$ due to the lattice expansion is calculated using

$$\Delta F_{expansion} = \int_1^{1.40} d\gamma \left\langle \sum_{i,j} \frac{\partial U(r_{ij})}{\partial r_{ij}} \frac{\partial r_{ij}}{\partial \gamma} \right\rangle_\gamma, \quad (7)$$

where the sum extends over all pairs of beads on different DNA-coated nanoparticles and $U(r_{ij})$ is the pair interaction between the beads. The Helmholtz free energy of the superlattice is given by

$$F = F_{reference} - \Delta F_{spring} - \Delta F_{expansion}, \quad (8)$$

where $F_{reference}$ is the free energy of the expanded reference state of non-interacting DNA-coated nanoparticles. Finally, the Helmholtz free-energy difference ΔF between the pBCT and SC crystals reads
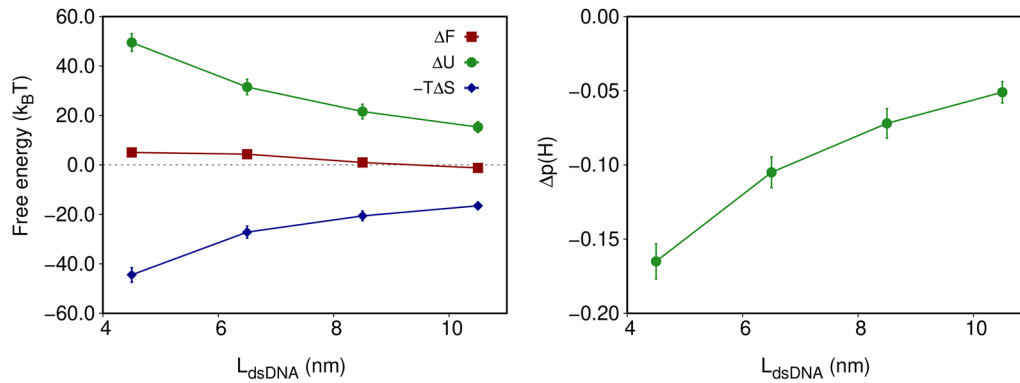
FIG. 12. (a) The entropy $-T\Delta S$ and internal energy ΔU contribution to the free-energy difference $\Delta F = F^{pBCT} - F^{SC}$ between pBCT and SC superlattices of dsDNA-AuNPs with a grafting density $\rho = 0.150$ strands/nm^2, as a function of the length L_{dsDNA} of the DNA. Error bars are smaller than the symbol size, when not shown. (b) The difference in the percentage of hybridizations $\Delta p(H)$ between pBCT and SC superlattices as a function of the length L_{dsDNA} of the DNA corresponding to the systems in (a); The internal energy can be measured by $\Delta U = U^{pBCT} - U^{SC} = 3\varepsilon_{bp}|\Delta p(H)|N_m$, where N_m the maximum number of hybridizations.

$$\Delta F = F^{pBCT} - F^{SC}$$
$$= \Delta F^{SC}_{spring} - \Delta F^{pBCT}_{spring} + \Delta F^{SC}_{expansion} - \Delta F^{pBCT}_{expansion}. \quad (9)$$

We then use the relationship $3\varepsilon\Delta p(H)N_m$[27,29] to measure ΔU. Here, $\varepsilon = 4.0k_BT$ represents the strength of the hybridization between non-self-complementary sticky ends, $\Delta p(H)$ is the difference in hybridizations between pBCT and SC crystal phases, and N_m is the maximum number of hybridizations. With the obtained values of ΔF and ΔU, we calculated the entropy contribution, as illustrated in Fig. 12.

We clearly observe from Fig. 12 that the free-energy difference between pBCT and SC crystal phases decreases from a positive to a negative value between a DNA length of $L_{dsDNA} \approx 8.5$ nm, indicating that the SC crystal is stable for $L_{dsDNA} < 8.5$ nm and the pBCT crystal is stable for $L_{dsDNA} > 8.5$ nm, as also found in Fig. 5(b). The transition from pBCT to SC is energetically favorable due to a high number of hybridization events between the relatively short DNA linkers. However, as the DNA strands become longer and more flexible, a phase transformation occurs from SC to pBCT due to a gain in entropy arising from the orientational degrees of freedom of the nanoparticles in the pBCT phase. This is supported by the decrease in $|\Delta p(H)|$ during the SC to pBCT transition, indicating a decrease in ΔU as shown in Fig. 12(b).

IV. CONCLUSIONS

In conclusion, we used a coarse-grained model of DNA-functionalized nanoparticles to investigate the shape-induced crystallization of a binary mixture of nanocubes with immobilized complementary DNA strands. By controlling the anisotropy of the shell of DNA ligands on the nanoparticle, the binary mixture of nanoparticles is programmed to self-assemble into SC, pBCT, and d-pBCT superstructures, while the DNA length, rigidity, and grafting density determined the orientation and lattice symmetry of the nanocubes. Our study revealed that the spatial distribution of the DNA hybridizations plays a crucial role in the transition from the SC phase to pBCT phase, and the orientational order decreases with decreasing grafting density or increasing DNA length. SC phases have been observed using spherical DNA-functionalized nanoparticles.[18] However, DNA-functionalized nanocubes can form new superlattice structures, pBCT and d-pBCT, due to the interplay between the anisotropic particle shape and ligand structure. These structures are not attainable with spherical particles. However, for DNA-functionalized nanocubes with very long spacers, the anisotropic particle shape and ligand structure would become less relevant, resulting in effectively spherical particles that could self-assemble into bcc superlattice structures.[18] Additionally, we found that the transition from pBCT to SC was energetically favorable due to the high hybridized interaction between short DNA-decorated nanoparticles. Conversely, longer and flexible DNA strands led to a phase transformation from SC to the pBCT phase due to a gain in entropy arising from the orientational degrees of freedom of the nanoparticles in the pBCT phase. These results can be extended to DNA-functionalized nanoparticles with various compositions, shapes, and sizes and have important consequences for the rational design of self-assembled structures based on geometric considerations.

AUTHOR DECLARATIONS

Conflict of Interest
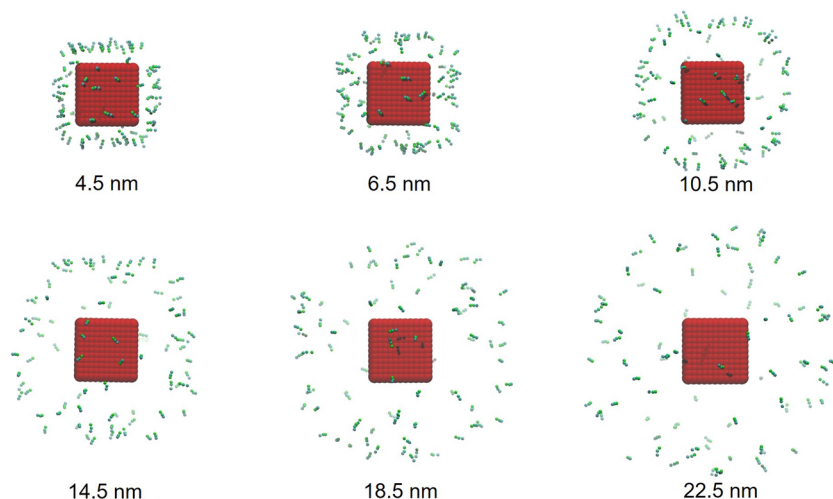
The authors have no conflicts to disclose.

FIG. 13. The spatial distribution of sticky ends on a single dsDNA-AuNP for varying DNA lengths as labeled.

Author Contributions

Yunhan Zhang: Conceptualization (equal); Data curation (equal); Formal analysis (equal); Investigation (equal); Methodology (equal); Software (equal); Validation (equal); Visualization (equal); Writing – original draft (equal); Writing – review & editing (equal). **Giuliana Giunta**: Methodology (equal). **Haojun Liang**: Conceptualization (equal); Funding acquisition (equal); Methodology (equal). **Marjolein Dijkstra**: Conceptualization (equal); Funding acquisition (equal); Project administration (equal); Resources (equal); Supervision (equal); Writing – original draft (equal); Writing – review & editing (equal).

DATA AVAILABILITY

The data that support the findings of this study are available from the corresponding author upon reasonable request.

APPENDIX: SPATIAL DISTRIBUTION OF STICKY ENDS FOR ISOLATED dsDNA-AuNPS

In Fig. 13, we plot the spatial distribution of sticky ends on a single dsDNA-AuNP for varying DNA lengths. As the DNA length increases from 4.5 to 22.5 nm, we clearly observe that the spatial distribution of sticky ends of a single dsDNA-AuNP becomes more spherical, explaining the loss in orientational order with increasing length of the spacers.

REFERENCES

[1] M. Dijkstra and E. Luijten, "From predictive modelling to machine learning and reverse engineering of colloidal self-assembly," Nat. Mater. **20**, 762–773 (2021).

[2] L. Adler-Abramovich, N. Kol, I. Yanai, D. Barlam, R. Z. Shneck, E. Gazit, and I. Rousso, "Self-assembled organic nanostructures with metallic-like stiffness," Angew. Chem., Int. Ed. **122**, 10135–10138 (2010).

[3] X.-B. Li, Y.-J. Gao, Y. Wang, F. Zhan, X.-Y. Zhang, Q.-Y. Kong, N.-J. Zhao, Q. Guo, H.-L. Wu, Z.-J. Li *et al.*, "Self-assembled framework enhances electronic communication of ultrasmall-sized nanoparticles for exceptional solar hydrogen evolution," J. Am. Chem. Soc. **139**, 4789–4796 (2017).

[4] J. F. Shin, W. Xu, M. Zanella, K. Dawson, S. N. Savvin, J. B. Claridge, and M. J. Rosseinsky, "Self-assembled dynamic perovskite composite cathodes for intermediate temperature solid oxide fuel cells," Nat. Energy **2**, 16214 (2017).

[5] Y. D. Park, A. T. Hanbicki, S. C. Erwin, C. S. Hellberg, J. M. Sullivan, J. E. Mattson, T. F. Ambrose, A. Wilson, G. Spanos, and B. T. Jonker, "A group-IV ferromagnetic semiconductor: Mn_xGe_{1-x}," Science **295**, 651–654 (2002).

[6] H. Wu, G. Chan, J. W. Choi, I. Ryu, Y. Yao, M. T. McDowell, S. W. Lee, A. Jackson, Y. Yang, L. Hu and Y. Cui, "Stable cycling of double-walled silicon nanotube battery anodes through solid–electrolyte interphase control," Nat. Nanotechnol. **7**, 310–315 (2012).

[7] C. A. Mirkin, "The polyvalent gold nanoparticle conjugate—Materials synthesis, biodiagnostics, and intracellular gene regulation," MRS Bull. **35**, 532–539 (2010).

[8] U. Agarwal and F. A. Escobedo, "Mesophase behaviour of polyhedral particles," Nat. Mater. **10**, 230–235 (2011).

[9] P. F. Damasceno, M. Engel, and S. C. Glotzer, "Predictive self-assembly of polyhedra into complex structures," Science **337**, 453–457 (2012).

[10] M. Dijkstra, "Entropy-driven phase transitions in colloids: From spheres to anisotropic particles," Adv. Chem. Phys. **156**, 35 (2014).

[11] M. A. Boles, M. Engel, and D. V. Talapin, "Self-assembly of colloidal nanocrystals: From intricate structures to functional materials," Chem. Rev. **116**, 11220–11289 (2016).

[12] S. Torquato and Y. Jiao, "Dense packings of the platonic and archimedean solids," Nature **460**, 876–879 (2009).

[13] J. de Graaf, R. van Roij, and M. Dijkstra, "Dense regular packings of irregular nonconvex particles," Phys. Rev. Lett. **107**, 155501 (2011).

[14] J. de Graaf, L. Filion, M. Marechal, R. van Roij, and M. Dijkstra, "Crystal-structure prediction via the floppy-box Monte Carlo algorithm: Method and application to hard (non) convex particles," J. Chem. Phys. **137**, 214101 (2012).

[15] C. A. Mirkin, R. L. Letsinger, R. C. Mucic, and J. J. Storhoff, "A DNA-based method for rationally assembling nanoparticles into macroscopic materials," Nature **382**, 607–609 (1996).

[16] A. P. Alivisatos, K. P. Johnsson, X. Peng, T. E. Wilson, C. J. Loweth, M. P. Bruchez, and P. G. Schultz, "Organization of "nanocrystal molecules" using DNA," Nature **382**, 609–611 (1996).

[17] D. Nykypanchuk, M. M. Maye, D. van der Lelie, and O. Gang, "DNA-guided crystallization of colloidal nanoparticles," Nature **451**, 549–552 (2008).

[18] R. J. Macfarlane, B. Lee, M. R. Jones, N. Harris, G. C. Schatz, and C. A. Mirkin, "Nanoparticle superlattice engineering with DNA," Science **334**, 204–208 (2011).

[19] M. R. Jones, R. J. Macfarlane, B. Lee, J. Zhang, K. L. Young, A. J. Senesi, and C. A. Mirkin, "DNA-nanoparticle superlattices formed from anisotropic building blocks," Nat. Mater. **9**, 913–917 (2010).

[20] C. R. Laramy, M. N. O'Brien, and C. A. Mirkin, "Crystal engineering with DNA," Nat. Rev. Mater. **4**, 201–224 (2019).

[21] W. B. Rogers, W. M. Shih, and V. N. Manoharan, "Using DNA to program the self-assembly of colloidal nanoparticles and microparticles," Nat. Rev. Mater. **1**, 16008 (2016).

[22] M. Girard, S. Wang, J. S. Du, A. Das, Z. Huang, V. P. Dravid, B. Lee, C. A. Mirkin, and M. Olvera de la Cruz, "Particle analogs of electrons in colloidal crystals," Science **364**, 1174–1178 (2019).

[23] X. Zhou, D. Yao, W. Hua, N. Huang, X. Chen, L. Li, M. He, Y. Zhang, Y. Guo, S. Xiao et al., "Programming colloidal bonding using DNA strand-displacement circuitry," Proc. Natl. Acad. Sci. U. S. A. **117**, 5617–5623 (2020).

[24] W. B. Rogers and V. N. Manoharan, "Programming colloidal phase transitions with DNA strand displacement," Science **347**, 639–642 (2015).

[25] Q. Yu, X. Zhang, Y. Hu, Z. Zhang, and R. Wang, "Dynamic properties of DNA-programmable nanoparticle crystallization," ACS Nano **10**, 7485–7492 (2016).

[26] C. Knorowski, S. Burleigh, and A. Travesset, "Dynamics and statics of DNA-programmable nanoparticle self-assembly and crystallization," Phys. Rev. Lett. **106**, 215501 (2011).

[27] T. I. N. G. Li, R. Sknepnek, and M. Olvera de la Cruz, "Thermally active hybridization drives the crystallization of DNA-functionalized nanoparticles," J. Am. Chem. Soc. **135**, 8535–8541 (2013).

[28] T. I. N. G. Li, R. Sknepnek, R. J. Macfarlane, C. A. Mirkin, and M. Olvera de la Cruz, "Modeling the crystallization of spherical nucleic acid nanoparticle conjugates with molecular dynamics simulations," Nano Lett. **12**, 2509–2514 (2012).

[29] G. Zhu, Z. Xu, Y. Yang, X. Dai, and L.-T. Yan, "Hierarchical crystals formed from DNA-functionalized Janus nanoparticles," ACS Nano **12**, 9467–9475 (2018).

[30] M. N. O'Brien, M. R. Jones, B. Lee, and C. A. Mirkin, "Anisotropic nanoparticle complementarity in DNA-mediated co-crystallization," Nat. Mater. **14**, 833–839 (2015).

[31] R. N. Kress and M. R. Jones, "Colloidal interactions get patchy and directional," Proc. Natl. Acad. Sci. U. S. A. **117**, 15382–15384 (2020).

[32] F. Smallenburg, L. Filion, M. Marechal, and M. Dijkstra, "Vacancy-stabilized crystalline order in hard cubes," Proc. Natl. Acad. Sci. U. S. A. **109**, 17886–17890 (2012).

[33] A. P. Gantapara, J. de Graaf, R. van Roij, and M. Dijkstra, "Phase diagram and structural diversity of a family of truncated cubes: Degenerate close-packed structures and vacancy-rich states," Phys. Rev. Lett. **111**, 015501 (2013).

[34] A. P. Gantapara, J. de Graaf, R. van Roij, and M. Dijkstra, "Phase behavior of a family of truncated hard cubes," J. Chem. Phys. **142**, 054904 (2015).

[35] R. D. Batten, F. H. Stillinger, and S. Torquato, "Phase behavior of colloidal superballs: Shape interpolation from spheres to cubes," Phys. Rev. E **81**, 061105 (2010).

[36] R. Ni, A. P. Gantapara, J. Dde Graaf, R. van Roij, and M. Dijkstra, "Phase diagram of colloidal hard superballs: From cubes via spheres to octahedra," Soft Matter **8**, 8826–8834 (2012).

[37] L. Rossi, S. Sacanna, W. T. M. Irvine, P. M. Chaikin, D. J. Pine, and A. P. Philipse, "Cubic crystals from cubic colloids," Soft Matter **7**, 4139–4142 (2011).

[38] J.-M. Meijer, A. Pal, S. Ouhajji, H. N. Lekkerkerker, A. P. Philipse, and A. V. Petukhov, "Observation of solid–solid transitions in 3D crystals of colloidal superballs," Nat. Commun. **8**, 14352 (2017).

[39] J. Henzie, M. Grünwald, A. Widmer-Cooper, P. L. Geissler, and P. Yang, "Self-assembly of uniform polyhedral silver nanocrystals into densest packings and exotic superlattices," Nat. Mater. **11**, 131–137 (2012).

[40] C. Avci, I. Imaz, A. Carné-Sánchez, J. A. Pariente, N. Tasios, J. Pérez-Carvajal, M. I. Alonso, A. Blanco, M. Dijkstra, C. López and D. Maspoch, "Self-assembly of polyhedral metal–organic framework particles into three-dimensional ordered superstructures," Nat. Chem. **10**, 78–84 (2018).

[41] A. Klinkova, H. Thérien-Aubin, A. Ahmed, D. Nykypanchuk, R. M. Choueiri, B. Gagnon, A. Muntyanu, O. Gang, G. C. Walker, and E. Kumacheva, "Structural and optical properties of self-assembled chains of plasmonic nanocubes," Nano Lett. **14**, 6314–6321 (2014).

[42] B. Gao, G. Arya, and A. R. Tao, "Self-orienting nanocubes for the assembly of plasmonic nanojunctions," Nat. Nanotechnol. **7**, 433–437 (2012).

[43] K. L. Gurunatha, S. Marvi, G. Arya, and A. R. Tao, "Computationally guided assembly of oriented nanocubes by modulating grafted polymer–surface interactions," Nano Lett. **15**, 7377–7382 (2015).

[44] W. H. Evers, B. Goris, S. Bals, M. Casavola, J. De Graaf, R. van Roij, M. Dijkstra, and D. Vanmaekelbergh, "Low-dimensional semiconductor superlattices formed by geometric control over nanocrystal attachment," Nano Lett. **13**, 2317–2323 (2013).

[45] J. J. Geuchies, C. Van Overbeek, W. H. Evers, B. Goris, A. De Backer, A. P. Gantapara, F. T. Rabouw, J. Hilhorst, J. L. Peters, O. Konovalov et al., "In situ study of the formation mechanism of two-dimensional superlattices from PbSe nanocrystals," Nat. Mater. **15**, 1248–1254 (2016).

[46] C. Anzivino, G. Soligno, R. van Roij, and M. Dijkstra, "Chains of cubic colloids at fluid–fluid interfaces," Soft Matter **17**, 965–975 (2021).

[47] G. Soligno and D. Vanmaekelbergh, "Understanding the formation of PbSe honeycomb superstructures by dynamics simulations," Phys. Rev. X **9**, 021015 (2019).

[48] G. Soligno, M. Dijkstra, and R. van Roij, "Self-assembly of cubic colloidal particles at fluid–fluid interfaces by hexapolar capillary interactions," Soft Matter **14**, 42–60 (2018).

[49] G. Soligno, M. Dijkstra, and R. van Roij, "Self-assembly of cubes into 2D hexagonal and honeycomb lattices by hexapolar capillary interactions," Phys. Rev. Lett. **116**, 258001 (2016).

[50] M. N. O'Brien, M. Girard, H.-X. Lin, J. A. Millan, M. Olvera de la Cruz, B. Lee, and C. A. Mirkin, "Exploring the zone of anisotropy and broken symmetries in DNA-mediated nanoparticle crystallization," Proc. Natl. Acad. Sci. U. S. A. **113**, 10485–10490 (2016).

[51] F. Lu, T. Vo, Y. Zhang, A. Frenkel, K. G. Yager, S. Kumar, and O. Gang, "Unusual packing of soft-shelled nanocubes," Sci. Adv. **5**, eaaw2399 (2019).

[52] J. A. Anderson, C. D. Lorenz, and A. Travesset, "General purpose molecular dynamics simulations fully implemented on graphics processing units," J. Chem. Phys. **227**, 5342–5359 (2008).

[53] T. D. Nguyen, C. L. Phillips, J. A. Anderson, and S. C. Glotzer, "Rigid body constraints realized in massively-parallel molecular dynamics on graphics processing units," Comput. Phys. Commun. **182**, 2307–2313 (2011).

[54] J. A. Anderson, J. Glaser, and S. C. Glotzer, "HOOMD-blue: A python package for high-performance molecular dynamics and hard particle Monte Carlo simulations," Comput. Mater. Sci. **173**, 109363 (2020).

[55] P. Bartlett and A. I. Campbell, "Three-dimensional binary superlattices of oppositely charged colloids," Phys. Rev. Lett. **95**, 128302 (2005).

[56] R. Mao, J. O'Leary, A. Mesbah, and J. Mittal, "A deep learning framework discovers compositional order and self-assembly pathways in binary colloidal mixtures," JACS Au. **2**, 1818–1828 (2022).

[57] G. Hou, X. Xia, J. Liu, W. Wang, M. Dong, and L. Zhang, "Designing superlattice structure via self-assembly of one-component polymer-grafted nanoparticles," J. Phys. Chem. B **123**, 2157–2168 (2019).

[58] M. X. Wang, J. D. Brodin, J. A. Millan, S. E. Seo, M. Girard, M. Olvera de la Cruz, B. Lee, and C. A. Mirkin, "Altering DNA-programmable colloidal crystallization paths by modulating particle repulsion," Nano Lett. **17**, 5126–5132 (2017).

[59] P. D. Duncan, M. Dennison, A. J. Masters, and M. R. Wilson, "Theory and computer simulation for the cubatic phase of cut spheres," Phys. Rev. E **79**, 031702 (2009).

[60] R. V. Thaner, Y. Kim, T. I. N. G. Li, R. J. Macfarlane, S. T. Nguyen, M. Olvera de la Cruz, and C. A. Mirkin, "Entropy-driven crystallization behavior in DNA-mediated nanoparticle assembly," Nano Lett. **15**, 5545–5551 (2015).

[61] E. J. Meijer, D. Frenkel, R. A. LeSar, and A. J. C. Ladd, "Location of melting point at 300 K of nitrogen by Monte Carlo simulation," J. Chem. Phys. **92**, 7570–7575 (1990).

[62] Z. Fan and M. Grünwald, "Orientational order in self-assembled nanocrystal superlattices," J. Am. Chem. Soc. **141**, 1980–1988 (2019).

[63] M. P. Howard, A. Z. Panagiotopoulos, and A. Nikoubashman, "Efficient mesoscale hydrodynamics: Multiparticle collision dynamics with massively parallel GPU acceleration," Comput. Phys. Commun. **230**, 10–20 (2018).

20 December 2023 10:05:40